Journal of Molecular Structure 1232 (2021) 129933

Contents lists available at ScienceDirect

Journal of Molecular Structure

journal homepage: www.elsevier.com/locate/molstr

Towards significant enhancement of structural and optoelectronic properties of porphyrin palladium(II) complex: A theoretical and experimental analysis

A.A.M. Farag[a,*], N. Roushdy[b], Shimaa Abdel Halim[c]

[a] Thin-film Laboratory, Physics Department, Faculty of Education, Ain Shams University, Roxy, Cairo, 11757, Egypt
[b] Electronic Materials Department, Advanced Technology and New Material Institute, City for Scientific Research and Technological Applications, New Borg El Arab City, 21934, Alexandria, Egypt
[c] Department of Chemistry, Faculty of Education, Ain Shams University, Roxy, 11711, Cairo, Egypt

ARTICLE INFO

Article history:
Received 16 November 2020
Revised 8 January 2021
Accepted 9 January 2021
Available online 12 January 2021

Keywords:
Thin films
Energy gap
NLO
DFT calculations
Photodetector

ABSTRACT

In the present investigation, the nanostructure of porphyrin palladium(II) complex thin films was fabricated by low-cost conventional thermal analysis. The experimental and simulation investigations were used for the analysis of the structure and the unique optical characteristics for optoelectronic applications. The simulation processes using TD-DFT/ B3LYP were implemented to extract the distinguished geometry optimizations and other related parameters. The quantum theory of atoms in molecules (QTAIM) was additionally applied for the studied complexes to evaluate their peculiar electronic features. An indexation of XRD was performed to give a full identification of the crystal structure and supported by the results of transmission electron microscopy images. The investigation of the surface morphology and its quality for the optical applications was established using the atomic force microscopy, AFM supported surface topography mapping images. The optical properties confirm two main direct transitions with determined band gaps of 2.31 and 2.98 eV. The experimental optical gap was comparable with those theoretically extracted using DFT. The characteristics of the current density-voltage measurements verified rectification in the dark and under different values of illuminations. The device showed remarkable rectification characteristics with good responsitivity under illumination conditions. The maximum external quantum efficiency of 9.8% was obtained and compared to other organic-based devices.

1. Introduction

Recently, there has been a renewed interest in the molecular materials that are essential for a wide range of technologies due to the characteristics of outstanding photonic response, rapid response interval, and easy operation for manufacturing optoelectronic devices [1–2]. Porphyrin dyes are a class of macrocycles consisting of four pyrrole units associated with methine bridges. The extremely π-conjugated system gives strong absorption in both ultraviolet and visible regions of the optical spectrum, great exciton diffusion length, facile molecular structure alteration [3]. The metal complexes of these structures were introduced in a large number of electronic and transport devices for various photonic and electronic applications [4]. The transition metalloporphyrin complexes have established comprehensive applications in various field of pharmaceutical agents, spectroscopy, chromatography, catalysts, sensor assembly, efficient photo converters, non-linear optics, optoelectronics, and smart materials [5,6].

The hybrid organic-inorganic structures represent an advanced alternative to design new materials as well as provides an enhancement for the development of pioneering manufacturing applications [7,8]. Numerous organic-inorganic hybrid –based porphyrin derivatives material based on Si substrate were previously studied [9–12]. El-Nahass et al. [9] have studied the current-voltage and capacitance-voltage as well as photovoltaic characteristics of Au/tetraphenylporphyrin (TPP)/n-type silicon heterojunction. Also, El-Nahass et al. [10] have considered the influence of both X-ray irradiation in the air on the characteristics of one of the metal substituted porphyrin (i.e. iron (III) chloride tetraphenyl porphyrin) films. Moreover, El-Nahass et al. [11] have studied the hybrid heterojunction cell of iron (III) chloride tetraphenyl porphyrin on p-type silicon. They recorded a rectification behavior and investigated the predominant conduction mechanisms and extracted some diode parameters. Cudia et al. [12] have presented an

* Corresponding author.
E-mail address: alaafaragg@edu.asu.edu.eg (A.A.M. Farag).

https://doi.org/10.1016/j.molstruc.2021.129933
0022-2860/

experimental investigation of the preparation and electronic characteristics of multilayer Zn-tetra-phenyl-porphyrin films on silicon substrates. They also confirmed the adequate structure of the proposed electronic spectrum. Zhang et al. [13] have investigated the fluorescence properties of the self-assembled ZnTPP monomers by scanning tunneling microscopy for assisting the scheming of the functional molecular optoelectronic devices. Furthermore, Balanay and Kim [14] have applied the theoretical calculations (i.e. DFT and TD-DFT) to porphyrin complexes (ZnTPP complexes) to obtain an efficient design of sensitizer in the application of one of the solar-type (i.e. dye-sensitized cells). They concluded that the efficiency of the obtained cells improves depending on the $\pi-$ conjugating properties and the capability of the electron-withdrawing of the substituents.

To best of our information, there are very few investigations of the experimental and theoretical of PaOEP thin films and their application for the optoelectronic devices have been carried out. Hence, the present work deals with the performance of PaOEP thin films supported by the geometrical and electronic structures by DFT theory at the B3LYB/SDD level. The main objective includes the preparation of the PaOEP thin films by low-cost conventional thermal evaporation method and diagnosis of the morphology and crystallinity using various technical methods. Also, the experimental measurements comprise the optical and electronic characteristics of the PaOEP thin films- based devices. The present descriptions contain three main parts: The first one involves the intensive study of the morphology and crystal structure of the prepared films, while part two includes DFT-theoretical calculations for investigating the optimized geometries and the role of the polarity of the desired solvents on the probable electronic transitions. The third part covers the electronic characteristics of the PaOEP thin film-device-based hybrid heterojunction characteristics and its sensitivity under influence of illumination for checking the capability of the device for the application as a photodiode.

2. Experimental

2.1. Thin-film and device preparation

The powder of 2,3,7,8,12,13,17,18- Octaethyl-21H,23H-porphine palladium(II) (Dye content 85.0%, Empirical Formula, $C_{36}H_{44}N_4Pd$, Molecular Weight 639.18) was purchased from Sigma- Aldrich (Merck) company, UK. PaOEP thin films were prepared using thermal evaporation technology, type Edward 306 Auto, Edwards Co., England) under a vacuum pressure of 10^{-4} Pa. Various types of pre-cleaned substrates include glass (appropriate for the structural characterization), corning glass (suitable for the optical characterization), and p-Si substrates (convenient for the device applications). The film thickness, homogeneity, and smoothness were controlled through the preparation processes. The quartz crystal monitor type Edwards FTM6 was used to control the rate of deposition through the preparation process (5 nm/s) and consequently the film thickness is about 300 nm. Rotating of the substrates through the deposition process enhances the homogeneity and the smoothing of the deposited films. To prepare the device, a good etching and cleaning of the p-Si substrate were performed using the main procedure detailed in the literature [15]. The ohmic contact on the p-Si backside was done by depositing In-film as a back contact electrode followed by the front contact by depositing a thin layer of Au on the PaOEP thin film.

2.2. characterizations methods

The structure characterization of the PaOEP samples was employed by using the SEM, type JEOL-JSM-636 OLA, for checking the morphology of the surface and its roughness characterization. The crystalline structure was considered by using TEM, type FEI TECNAI G20 working at 200 kV. The crystallinity properties of PaOEP samples were engaged by using Shimadzu XRD 7000 with a copper target, $\lambda_{CuK\alpha} = 0.15406$ nm, and nickel target. The applied voltage of the XRD instrument is 30 kV with a current of 30 mA and a scan rate of 2°/min for covering the scan range of 4–90°

The spectra of the photoluminescence, PL of the samples were achieved by using PL spectrometer type RF-5301.

The spectral dependence of the absorption of the prepared samples was investigated using a spectrophotometer, type JASCO 670.

The electrical characteristics of the device, represented as current-voltage properties were examined by a full-computerized Keithly 2635 A. The devices were illuminated by various light intensities at room temperature (i.e. 300 K) and measured by type TM-306, solar power meter instrument.

2.3. Computational method

The full geometry optimizations of PaOEP were supported by using B3LYP at the SDD level [16–18] and LANL2DZ level [19–22]. The localization of the frontier orbitals was also considered. All computations were achieved using Gaussian 09 W software package [23] supported by the visualization using GaussView 5.0.9 [24] and/or chem craft 1.6 [25]. Besides, FT-IR-vibrational spectrum assignments of PaOEP based on the computationally predicted were investigated. Also, the geometrical properties and the expected absorption spectra of the structure in various solvents were calculated by CAM-B3LYP at LANL2DZ [26]. The topological analysis of the electron density distribution function r(r) at the Bader·s level of a quantum theory of atoms in molecules (QTAIM) [27], was achieved for the optimized structures of PaOEP structure. The energies of the coordination Pd–N bonds was calculated using the Espinosa equation as follows [28]:

$$E = 0.5\,\upsilon(r), \tag{1}$$

where E is the bond energy (a.u.) and $\upsilon(r)$ is the potential energy density (a.u.) at the corresponding (3,−1) critical point [27]. The above relationship is broadly used for the energy estimation of different types of hydrogen van der Waals, coordination, and homopolar bonds [28]. The usage of the Bader method makes it possible to describe qualitatively the chemical bond nature based on the signs and values of the electron density Laplacian $\nabla^2\rho(r)$ and of the electron energy density $h_e(r)$ at the corresponding (3, −1) bond critical point using the following conditions [27,29]:

(1) $\nabla^2\rho(r) < 0$ and $h_e(r) < 0$ indicate the shared interactions, i.e. weakly polar and nonpolar covalent bonds;
(2) $\nabla^2\rho(r) > 0$ and $h_e(r) < 0$ indicate the intermediate interactions, which include strong hydrogen bonds and most of the coordination bonds;
(3) $\nabla^2\rho(r) > 0$ and $h_e(r) > 0$ indicate the closed-shell interactions such as weak hydrogen bonds, van der Waals interactions, and ionic bonds.

The binding energy (BE) of a metal cation Pd to the OEP based ligand was also calculated by the following equation in the framework of the DFT/B3LYP additive scheme in a gas phase:

$$BE = E(Pd - OEP\,complex) - \left[E\left(Pd^{+2}\right) + E(OEP - ligand)\right] \tag{2}$$

Counterpoise (CP) corrections were applied to all binding energy values to avoid basis set superposition errors (BSSEs) [30]. The QTAIM calculations have been carried out using the AIM All program package [31].

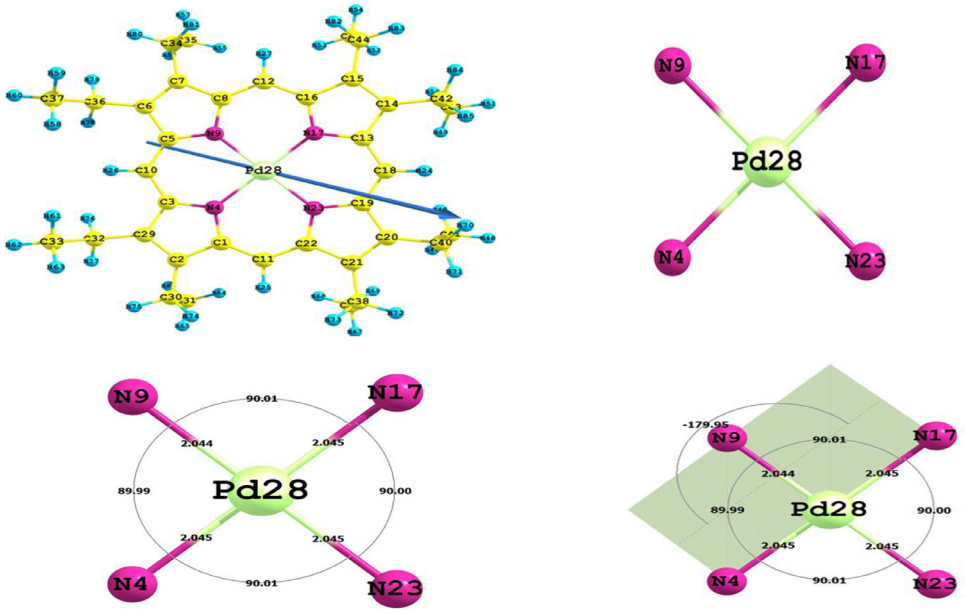

Fig. 1. Optimized geometry, numbering system, bond lengths, bond angles, dihedral angle and vector of dipole moment for 2,3,7,8,12,13,17,18-Octaethyl-21H,23H-porphine palladium(II) using B3LYP/ LANL2DZ.

3. Results and discussion

3.1. Molecular orbital calculations

3.1.1. Geometrical parameters

The theoretical calculations using DFT and TD-DFT calculations were used for modeling the PaOEP structure, for an efficient sensor design of dye-sensitive solar cells. For the calculating of the PaOEP geometry and other related parameters, the simulation processes were achieved by using the hybrid function/LANL2DZ. Moreover, the charge separation is important attention for consideration due to its controlling the efficiency of the solar cell [32,33].

Fig. 1 presents the optimized geometry and most of the related parameters of the PaOEP using the B3LYB/SDD level. The analysis of Fig. (1) shows that: In the studied structure, Pd metal forms asymmetric bonds with N4, N9, N17, and N23 to create a complex. The coordinate covalent bond length between the Pd metal ion and the free dye (M-N) is very long compared to the typical bond length of M-L(i.e.metal-ligand) [34]. The very long M-N bonds indicate the ionic nature of these bonds. The calculated bond angles between the Pd metal ion and the binding sites in the coordination system, shown in Fig. 1 are found to be 90° that consistent well with those published experimental results of a similar structure [35]. The calculated dihedral angles around Pd^{+2} in the structure of PaOEP are near to 0° or indicates that the metal ion is located at the same level as the donation sites.

3.1.2. Ground-state properties and global reactivity descriptors

Fig. 2 shows the HOMO-LUMO energy gap value of the PaOEP structure obtained using B3LYB/SDD and B3LYP/ LANL2DZ. All the main extracted parameters were tabulated and listed in Table 1. The scaling factors were extracted and the calculated value of ZPVE and the total entropy were found to be 449.45552, 450.45624 kcal.mol^{-1}, and 243.982, 242.992 cal/mol. K, respectively, and scheduled in Table 1**.** The HOMO- LUMO energy gap was calculated by B3LYP / SDD, B3LYP/ LANL2DZ, and found to be 3.057, 3.052 eV, and shown in Fig. 2. While HOMO· s is π orbitals localized above Pd-metal ion, LUMO· s is π^* orbitals localized over the porphyrin rings. The HOMO–LUMO energy gap of the porphyrin ring may be lower under the influence of Pd-metal ion and octaethyl groups. This indicates that the intensity of the state may be less abundant close to the Fermi levels

Table 1
The optimized calculations of **PaOEP** structure at the B3LYP/SDD and B3LYP/ LANL2DZ.

Parameters	Values
Total Energy,(E_T)	−1745.1711
Zero Point Vibrational Energy	449.45552
	0.08107
Rotational constant	0.08058
	0.04199
Total Entropy	243.982
Translational	44.356
Rotational	37.551
Vibrational	162.075
Energy of the highest occupied molecular orbital (E_{HOMO})	−5.062192
Energy of the lowest unoccupied molecular orbital (E_{LUMO})	−2.005456
Energy Gap,(E_g)	3.056736
Dipole moment, (μ)	0.4039
I *(eV)*	5.062192
A*(eV)*	2.005456
X*(eV)*	3.533824
V*(eV^{-1})*	−3.533824
η*(eV)*	1.528368
S*(eV^{-1})*	0.327146
ω (eV)	4.085375

The results of the small η value of PaOEP reveals the charge-carrying capability of octa-ethylprophene groups, with an aporphine ring. While its chemical softness (S) shows the reveres tendency, tabulated in Table 1. According to the η values, the higher the η values, the harder the molecule and vice versa. Accordingly, the charge transfer follows more easily in the dye complex. The results show that a decrease of electronegativity (χ) due to the increasing of CT within the molecules. Moreover, the lower energy gap of PaOEP indicates an easier probability for electron transfer between the energy levels. Accordingly, the respective chemical hardness (η) is low while the electrophilicity(ω) is found to be high.

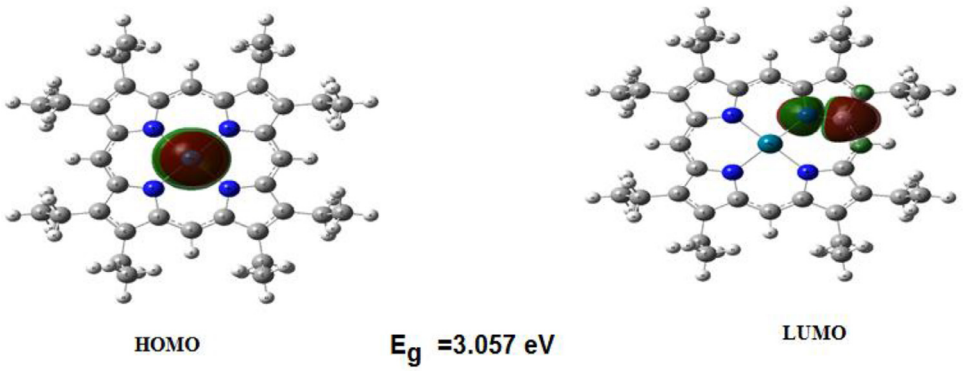

Fig. 2. HOMO, LUMO maps, energy gap of 2,3,7,8,12,13,17,18-Octaethyl-21H,23H-porphine palladium(II) using B3LYP/ LANL2DZ.

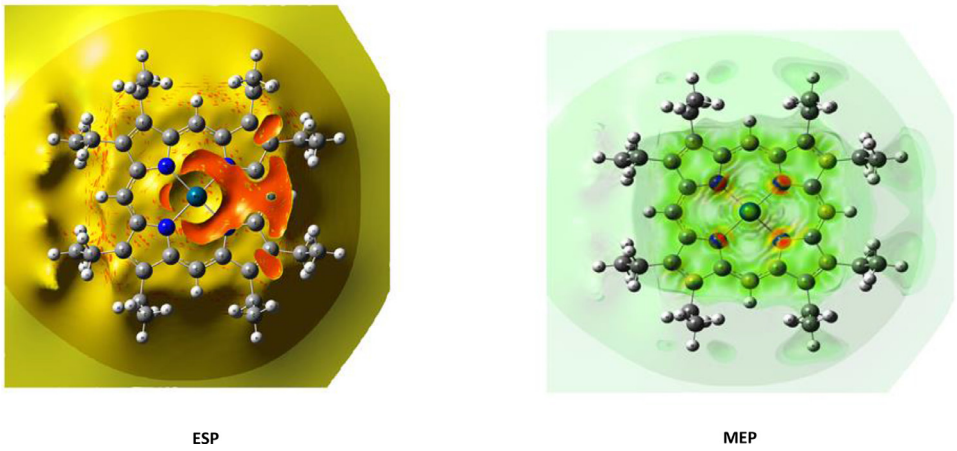

Fig. 3. ESP and 3D-MEP for 2,3,7,8,12,13,17,18-Octaethyl-21H,23H-porphine palladium(II) using B3LYP/ LANL2DZ.

3.1.3. Molecular electrostatic potential (MEP)calculation

The MEP contours have been briefly defined as a guide to understanding and expecting molecular performance [36–40]. It has proved to be a beneficial appliance in the study of electrophilic and nuclear procedures [36,41]. The color scheme of the MEP surface can be explained as follows: the cloud of red denotes the partially negative charge. Besides, the blue for expressing the lack of an electron. While the partially positive charge is indicated by the light blue. The slight electron deficiency was expressed by the yellow color. The slightly electron-rich region expresses the neutral green. Fig. 3 illustrates the MEP profiles of the PaOEP structure. The blue cloud indicates the intensity of the high positive potential that is influenced by the adding of the metal (Pd). The high positive potential is significantly grown in the octaethyl porphine region. The red cloud indicates the negative potential and confirms that the MEPs of the dye are influenced by the adding of the octaethyl groups. The low negative was significantly grown in the region of octaethyl sets. This means that the PaOEP body is more qualified for nucleophilic processes than those of the electrophilic. It turns out that the delocalization of the negative charge near the octaethyl groups participating in the supreme PV performance of PaOEP.

3.1.4. Charges population analysis

The description of the charges distribution and its related parameters and Lewis and non-total Lewis are tabulated in Table 2(a) and **(b)**. The utmost electronegative charges of −0.52985, −0.53110, −0.53160, −0.53043, and −0.58160 are grouped into the N4, N9, N17, N23, and Pd-atoms. These electrostatic atoms in the coordination field are inclined to contribute the electrons to the central Pd^{+2}. Moreover, normal population examination exhibited that 334 electrons in the PaOEP are dispersed over sub-shells.

According to NBO analysis, Table 2(a) shows up that the structure of the valence orbital of **Pd** is characterized by 4d5s. Regarding the core electrons, Table 2(b) shows that LANL2DZ provides approximately 88 electrons regardless of the structure of the ligand. Whereas the Rydberg orbitals (5p5d6p), account for the more extended bits of the base's functions used including polarization functions electrons. Their occupancies within the complexes are low and constant with 0.64 electrons except for the Pd atom that does not display any value. We can assume that the Rydberg electrons are certainly related to the presence of ligands. Almost the same remark concerns the valence electrons where only the Pd atom displays 9.40 electrons while all complexes show almost 7.42 electrons. Regarding the total electrons in palladium atom that is 45 when it is isolated. Consequently, we can admit that these results tend to highlight the electron donor's strength of the **OEP** ligand to **Pd**. The nominal charge of **Pd** in the **PaOEP** structure complex is +2. So, the natural atomic charge that corresponds to the difference between the nuclear charge of **Pd** (45) and its total electron population in Table 2(b) within the complex is very low (lower than +2) confirming a significant transfer of electron density from the ligands to **Pd**.

3.1.5. QTAIM analysis of pd –N interactions of paoep

Additional analysis of the nature of metallic bonding was performed within the formalities of Bader's theory [27] for PaOEP structure. Table 4, lists the critical points of Pd-N bonds that are characterized by positive values of Laplacian electron density $\nabla^2\rho(r) > 0$ and negative values of electron energy density Cremer-

Table 2a
Natural Charge, Natural Population, Natural population of Natural electronic Configuration of active sites of **PaOEP** at the B3LYP/ LANL2DZ.

Atom No.	Natural Charge	Natural Population				Natural electronic Configuration
		Core	Valence	Rydberg	Total	
N4	-0.52985	1.999	5.512	0.0189	7.530	[core]2S(1.33)2p(4.18)3p(0.02)
N9	-0.53110	1.999	5.513	0.0189	7.531	[core]2S(1.33)2p(4.18)3p(0.02)
N17	-0.53160	1.999	5.514	0.0189	7.532	[core]2S(1.33)2p(4.18)3p(0.02)
N23	-0.53043	1.999	5.512	0.0189	7.530	[core]2S(1.33)2p(4.18)3p(0.02)
Pd	-0.58160	35.99	9.405	0.02604	45.42	[core]4d(8.77)5p(0.24)6S(0.39)5d(0.01)6d(0.01)

Table 2b
Total charge analysis of **PaOEP** structure at the B3LYP/ LANL2DZ.

Effective Core	Core	Valence Lewis	Total Lewis	Valence non-Lewis	Rydberg non-Lewis	Total non-Lewis
28.000000	87.95 (99.94% of 88)	209.989 (96.33% of 218)	325.94 (97.587% of 334)	7.42 (2.220% of 334)	0.64 (0.19% of 334)	8.05871(2.413% of 334)

Table 3
Bond length (d) and selected topological parameters of the electron density distribution function ρ(r) of the **Pd–N** bond.

Parameters	Values
S(spin)	0
Bond	**Pd^{+2}–N**
d, A^0	2.051
ρ(r), e x a_0^{-3}	9.701×10^{-2}
υ(r), a.u.	-0.1550
g(r), a.u.	0.1400
h_e(r)[a], a.u.	-0.015
$\nabla^2\rho$(r), e x a_0^{-5}	0.5160
E, kcal mol^{-1}	-47.98
BE^b, kcal mol^{-1}	202.857
$BE^{b/n}$, kcal mol^{-1}	50.7141
BE^c, kcal mol^{-1}	206.045

$h_e(r)^a = \upsilon(r) + g(r)$, where g(r) is the kinetic energy density at the (3, _1) critical point; $1/4\ \nabla^2\rho(r) = 2g(r) + \upsilon(r)$. [b] BSSE corrected. [c] BSSE uncorrected binding energy of cations to the **OEP**-ligand at 0 K calculated by the DFT/B3LYP/ LANL2DZ approach in a gas phase without zero-point energy (ZPE) correction; n is the number of the equivalent coordination **Pd–N** bond (n = 4 for complex **PaOEP**).

Table 4
Total static dipole moment ($\boldsymbol{\mu}$), the mean polarizability (<$\boldsymbol{\alpha}$>), the anisotropy of the polarizability ($\boldsymbol{\Delta\alpha}$), and the mean first-order hyperpolarizability (<$\boldsymbol{\beta}$>), of **PaOEP** structure.

Property	Values
$\boldsymbol{\mu_x}$, D	0.2930
$\boldsymbol{\mu_y}$, D	−0.0959
$\boldsymbol{\mu_z}$, D	−0.2610
$\boldsymbol{\mu}$, **D**ebye [a]	0.4039
$\boldsymbol{\alpha_{XX}}$, a.u.	−224.7247
$\boldsymbol{\alpha_{XY}}$, a.u.	−0.0055
$\boldsymbol{\alpha_{YY}}$, a.u.	−224.8875
$\boldsymbol{\alpha_{ZZ}}$, a.u.	−269.3587
$\boldsymbol{\alpha_{YZ}}$, a.u.	−0.0144
$\boldsymbol{\alpha_{XZ}}$, a.u.	−3.4031
$\boldsymbol{<\alpha>} \times 10^{-24}$ esu	44.213
$\boldsymbol{\Delta\alpha} \times 10^{-24}$ esu	51.350
$\boldsymbol{\beta_{xxx}}$, a.u.	3.8706
$\boldsymbol{\beta_{xxy}}$, a.u.	0.1005
$\boldsymbol{\beta_{xyy}}$, a.u.	1.2178
$\boldsymbol{\beta_{yyy}}$, a.u.	−0.2834
$\boldsymbol{\beta_{xxz}}$, a.u.	5.2011
$\boldsymbol{\beta_{xyz}}$, a.u.	0.0639
$\boldsymbol{\beta_{yyz}}$, a.u.	8.7926
$\boldsymbol{\beta_{xzz}}$, a.u.	−0.0043
$\boldsymbol{\beta_{yzz}}$, a.u.	−0.0419
$\boldsymbol{\beta_{zzz}}$, a.u.	1.8404
$<\boldsymbol{\beta}> \times 10^{-30}$ esu[b]	3.5861

a, b Urea equal (1.3197D, 0.1947esu) results are taken from references [28].

Kraka h_e(r) < 0 which permits us to ascribe Pd - N bonds to a midway type of interaction. The degree of concentration of the electron density between the atoms defines the energy of the consistent reactions. Accordingly, **Pd^{2+}–N** bonds have higher binding energy values that determine the greater stability of **$[Pd\text{-}(OEP)]^{2+}$** in the ground single state. Generally, the binding energy (BE) values for "**Pd – OEP**" systems computed by the direct DFT method correlate well with the QTAIM predictions. Though, the BE values are considerably higher than the summation of the corresponding Pd-N bond energies extracted from QTAIM analysis (Table 3) as detected in the BE of s-block metal complexes [42]. These large differences in binding energy were clarified by the numerous methods of calculating BE. In the case of the DFT method, the dissolution energy is ignored (the calculation of the melt energy allows the BE to be reduced [43]) but it needs a lot of computational time, so these calculations have not been implemented in the present work). In contrast, the estimation of the complex energy by Bader's algorithm is based on the computation of the energy density potential at the critical point of the corresponding bond (3, 1). In this case, the melt energy has a negligible contribution, since the values of υ (r) are slightly dependent on the dissolution effect.

3.2. Morphology and crystalline characteristics

The surface morphology of the material is a significant feature and plays an imperative role in determining the mechanical, thermal, optical, and electrical properties of materials used in many modern technologies like optoelectronic [44]. The key topographic parameters like film surface roughness, crystallinity, particle size, surface porosity, are used for controlling the optoelectronic applications [45]. The top view of the surface topography of PaOEP was investigated by atomic force microscopy, AFM as shown in Fig. 4(a). This figure shows that the surface is heavily coated by PaOEP and the distributed particles of different shapes with diverse sizes. Moreover, the observed grain sizes all over the surface have a distinctive nano-scaled with a corrugated morphological characteristic. In Fig. 4(b) typical profiles, before (dark line) and after (gray line) filtration procedure, are shown. The line profile, shown in Fig. 4(b), clarifies a roughness distribution of PaOEP with an average root mean square, R_{rms} of 15 nm. Belfedal et al. [46] have concluded that the surface roughness of the materials is correlated to the microstructure of crystalline grains and indicated that the thickness of the film affects the surface roughness using the optical reflectance measurements. The 3-D AFM image of 5 × 5 μm^2 sizes is shown in Fig. 4(c). Moreover, the histogram of the grain

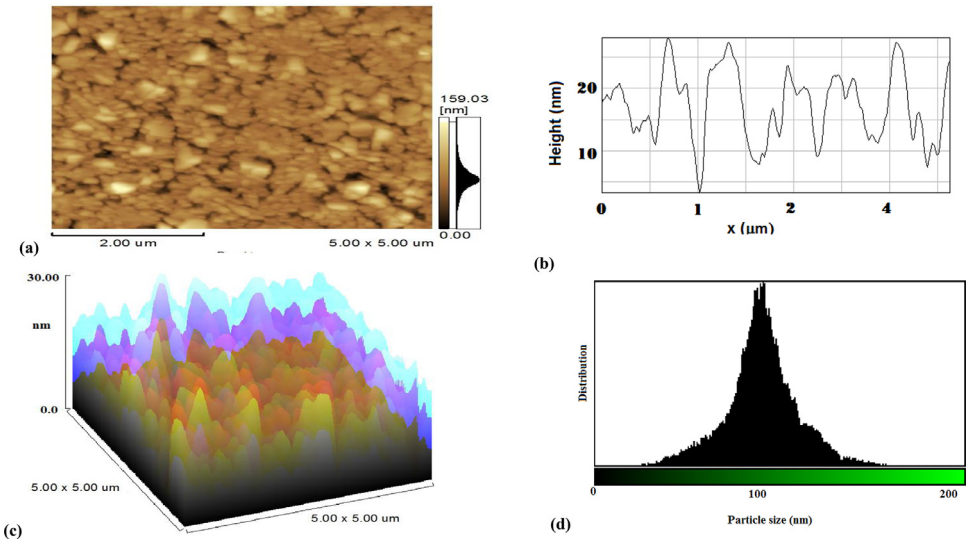

Fig. 4. AFM images and analysis (a) 2 D image, (b) 3D of AFM images, (c) roughness tracer analysis, and (d) particle size distribution of PaOEP structure.

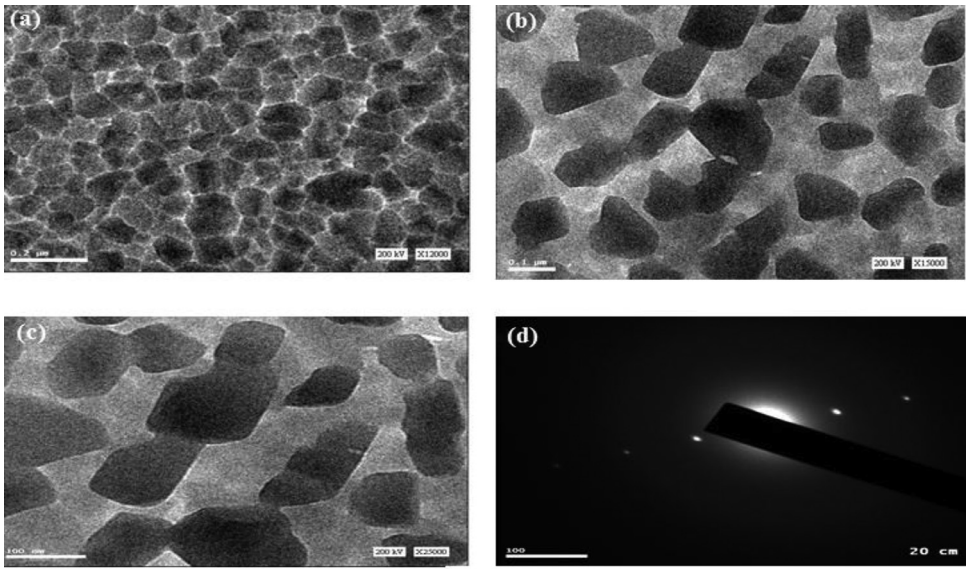

Fig. 5. (a-c) TEM images of different magnifications, and (d) SAED image of PaOEP structure.

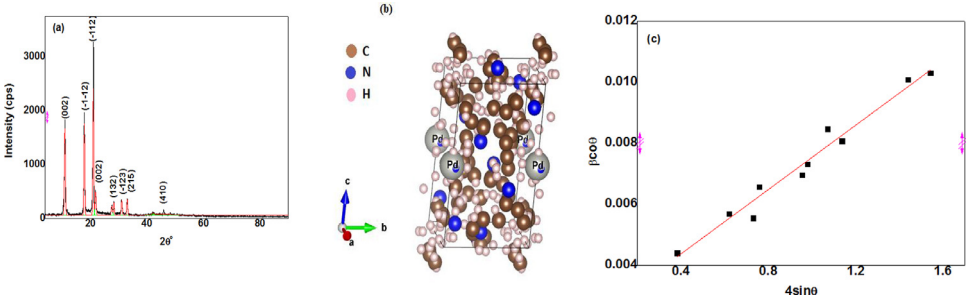

Fig. 6. (a) XRD pattern, (b) Plot The crystal structure of OEPP, and (c) Plot of $\beta\cos\theta$ vs. $4\sin\theta$ of PaOEP structure.

size distribution of PaOEP, shown in Fig. 4(d) specifies an average grain size of 100 nm.

The crystallinity characterization of PaOEP samples was also tested using the TEM micrograph. Fig. 5**(a)–(c)** shows a TEM micrograph with different magnifications. A well-crystal with a definite structure was obtained with an average crystallite size of 60–80 nm. The selected area electron diffraction, SAED of PaOEP, shown in Fig. 5**(d)**, confirms a typical ring pattern of a polycrystalline nature of the prepared films.

The crystallization of PaOEP samples is also studied by using the XRD technique. The XRD pattern is shown in Fig. 6**(a)**. The figure illustrates certain diffraction peaks emphasizing a polycrystalline nature. The obtained result agrees with those obtained from the TEM results. The diffraction pattern was indexed by utilizing

Table 5
Experimental and computational calculated of FTIR analysis of **PaOEP** at the B3LYP/ LANL2DZ.

No.	Wave number		IR Intensity		Assigments	References
	un-scaled	scaled	Rel.	Abs.		
1	3131	3009	21.83	12.84	υ C–H aromatic	[29]
2	3043	2925	26.22	16.72	υ C–H aliphatic	[29]
3	1538	1479	88.16	42.26	υ $C=N$ and β $C=C$ (in ring)	[29]
4	730	701	78.57	52.36	υ (M–N)	[30]

υ (Stretching); υ_2(Symmetric stretching); υ_3(Asymmetric stretching); β (In plane bending).

the Rietveld refinement program reinforced by a pseudo-Voigt profile [47] for obtaining the best fitting peak simulation. Accordingly, the lattice constants were considered and found to be $a = 8.126$ Å, $b = 9.626$ Å, $c = 16.547$ Å, α=78.66°, β=82.918°, γ=65.153° with the triclinic system, shown in Fig. 6**(b)**. The main crystal structure parameters like the microstrain and the mean crystallite size, were evaluated using the slope and intercept through the plot of $\beta\cos\theta$ vs. $4\sin\theta$ (i.e.Williamson –Hall plot) [48], shown in Fig. 6**(c)**. The linear fitting of the plot supports the homogeneity of the crystalline planes with uniform deformation. The extracted average crystallite size and microstrain are found to be 61.39 nm and 5.27×10^{-3}, respectively.

3.3. Non-linear optical calculations

Polarization characterizes the interaction of the structure under the influence of the applied field and is used for the determination of some important parameters listed in the literature [49,50]. The importance of linear polarization and first-order hyperpolarization are the basis for most applications [51]. The total static dipole moment, μ, the mean polarizability, $<\alpha>$, the anisotropy of the polarizability, $\Delta\alpha$, and the mean first-order hyperpolarizability, $<\beta>$ were extracted using B3LYP/SDD, B3LYP/ LANL2DZ and listed in Table 5. Urea is an accurately selected reference due to the leakage of the available applied data of PaOEP [52,53].

3.4. Vibration assignments of PaOEP structure

The vibration frequencies calculated at B3LYP/SDD, B3LYP/ LANL2DZ, and the related assignments using the FT-IR spectrum of PaOEP are listed in Fig. 7 and Table 6. The determined scale factor was determined and found to be 0.9613 at B3LYP/SDD basis set. The detailed assignments of PaOEP can be accomplished

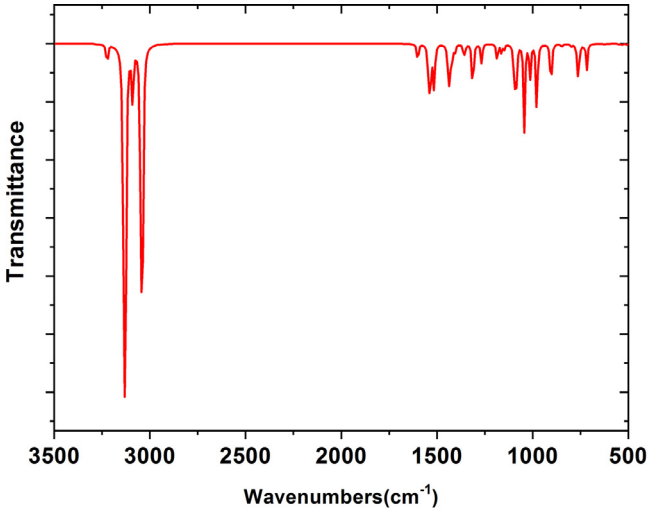

Fig. 7. Calculated IR spectra for PaOEP using B3LYP/ LANL2DZ.

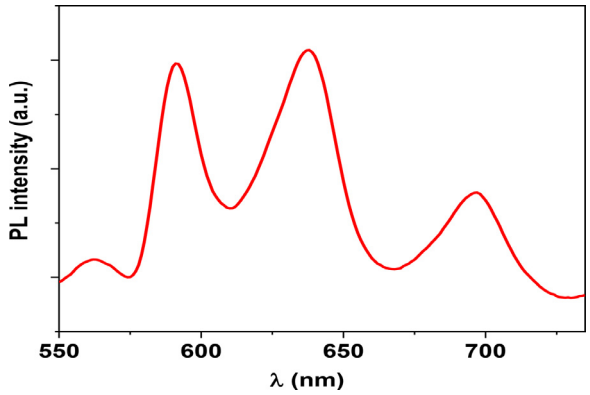

Fig. 8. Photoluminescence spectrum PaOEP using B3LYP/ LANL2DZ.

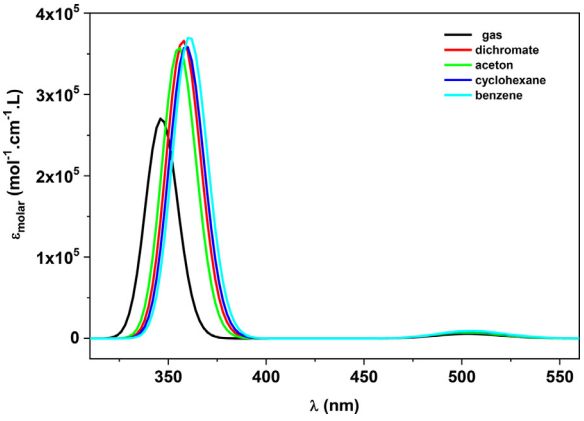

Fig. 9. Electronic absorption spectra of PaOEP using B3LYP/ SDD.

as follows: the stretching vibration of C–H (aromatic) are detected at 3000–3100 cm^{-1} [54] while the calculated vibration is found at 3131, 3130 cm^{-1} and assigned to aromatic stretching vibrations C–H aromatic stretching vibrations. The computed band at 2925, 2927 cm^{-1} is assigned to symmetric C–H aliphatic stretching vibration in CH_3. The vibration at 1480–1630 cm^{-1} is assigned to the $C=C$ vibrations [38]. The vibrations at 1538, 1536 cm^{-1} and 1479, 1781 cm^{-1} are assigned to stretching vibration of $C=C$ and $C=N$. Finally, the bands at 730, 732, and 701, 705 cm^{-1} are allocated to ν (M–N) stretching frequencies [55].

3.5. Photoluminescence (PL)characterization

The spectrum of PL of the studied structure was achieved utilizing 350 nm for the applied excitation wavelength. The emission spectrum is shown in Fig. 8. The figure confirms certain distinct characterized emission peaks in the visible region centered at 591.5, 638.2, and 696.6 nm. The main emission peaks recorded at 638.2 and 696.6 nm agree with those published for most porphyrins and their derivatives [56–58]. These peaks can

Table 6
Computed excitation energies (in eV),and absorption parameters of the **PaOEP** in vacuum computed at the CAM- B3LYP/ LANL2DZ level of theory.

Medium	Transition	Excitation energies	Type of transition	$\lambda_{max/nm}$	Oscillator strengths (f)	Configuration composition corresponding transition orbital
Gas phase	5	2.22	n-π^*	560	0.0217	0.44 (152 ->155); 0.55(153 ->154)
	6	2.46	n-π^*	503	0.0202	−0.44 (152 ->154); 0.54(153 ->155)
	20	3.58	π-π^*	347	1.0091	0.12 (147 ->154); −0.11(149 ->155); 0.52(152 ->154); 0.44(153 ->155)
Acetone	5	2.24	n-π^*	553	0.0271	0.19 (152 ->154); 0.39(152 ->155); −0.50(153 ->154); 0.24(153 ->155)
	6	2.47	n-π^*	506	0.0207	0.39 (152 ->154); −0.19(152 ->155); 0.24(153 ->154); 0.50(153 ->155)
	19	3.50	π-π^*	355	1.3274	0.53 (152 ->154); 0.11(152 ->155); −0.42(153 ->155);
	20	3.49	π-π^*	350	1.3161	−0.11 (152 ->154); 0.53(152 ->155); 0.42(153 ->155);
Benzene	5	2.23	n-π^*	556	0.0337	−0.12 (152 ->154); −0.41(152 ->155); 0.53(153 ->154); −0.16(153 ->155)
	6	2.46	n-π^*	504	0.0315	0.41 (152 ->154); −0.12(152 ->155); 0.16(153 ->154); 0.53(153 ->155)
	19	3.46	π-π^*	365	1.3774	0.54 (152 ->154); −0.43(153 ->155)
	20	3.44	π-π^*	360	1.3755	0.54 (152 ->154); 0.43(153 ->155)
Hexane	5	2.24	n-π^*	557	0.0325	−0.16 (152 ->154); −0.40(152 ->155); 0.51(153 ->154); −0.21(153 ->155)
	6	2.47	n-π^*	505	0.0323	0.40 (152 ->154); −0.16(152 ->155); 0.21(153 ->154); 0.51(153 ->155)
	19	3.45	π-π^*	360	1.3342	0.54 (152 ->154); −0.43(153 ->155)
	20	3.43	π-π^*	359	1.3320	0.54 (152 ->154); 0.43(153 ->155)
Dichloromethane	5	2.24	n-π^*	554	0.0292	0.18 (152 ->154); 0.39(152 ->155); −0.51(153 ->154); −0.23(153 ->155)
	6	2.46	n-π^*	503	0.0290	0.39 (152 ->154); −0.18(152 ->155); 0.23(153 ->154); 0.51(153 ->155)
	19	3.45	π-π^*	360	1.3342	0.53 (152 ->154); 0.11(152 ->155); −0.42(153 ->155)
	20	3.43	π-π^*	359	1.3320	−0.11 (152 ->154); 0.53(152 ->155); 0.42(153 ->154)

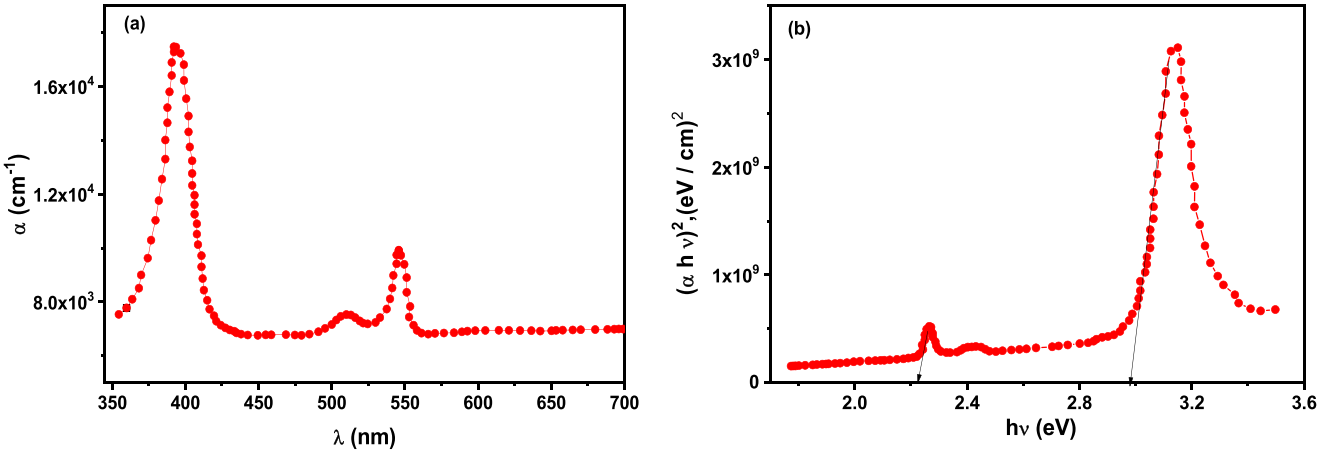

Fig. 10. (a) Spectral dependence of absorption coefficient, and (b) Plot of $(\alpha h\nu)^2$ vs. $h\nu$ of PaOEP structure.

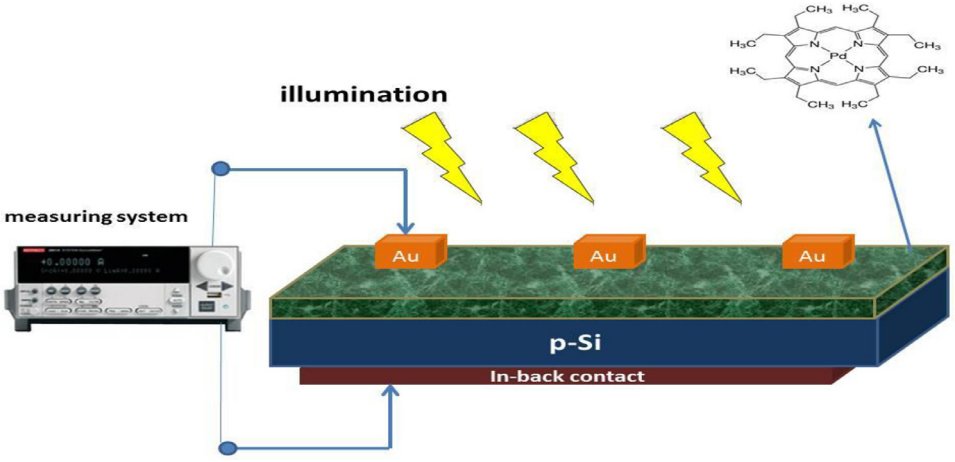

Fig. 11. Schematic diagram of Au/ PaOEP /p-Si /In heterojunction structure.

Table 7
A comparative analysis of 2,3,7,8,12,13,17,18-Octaethyl-21H,23H-porphine palladium(II) with similar type of compounds.

Parameters	2,3,7,8,12,13,17,18-Octaethyl-21H,23H-porphine palladium(II)at DFT/B3LYP/SDD	Ref. [1]at DFT/B3LYP/SDD	Ref. [2]at DFT/B3LYP/6–311G	Ref. [3]at DFT/B3LYP/6–31G(d,p)	Ref. [4]at DFT/CAM-B3LYP/6–31G(d,p)	Ref. [5]at DFT/B3LYP/6–31G(d)
E_{HOMO} (eV)	−5.062	−5.001	−6.108	−4.751	−5.980	−6.690
E_{LUMO} (eV)	−2.005	−2.530	−2.091	−1.751	−1.350	−2.170
E_g (eV)	3.057	2.471	4.017	3.000	4.630	4.520
(μ) Debye	0.404	0.002	9.760	0.595	5.213	6.524
I *(eV)*	5.062	5.001	6.108	4.751	5.980	6.690
A*(eV)*	2.005	2.530	2.091	1.751	1.350	2.170
X*(eV)*	3.534	3.766	4.099	3.251	3.665	4.430
V*(eV)*$^{-1}$	−3.534	−3.766	−4.099	−3.251	−3.665	−4.430
η*(eV)*	1.528	1.236	2.008	1.500	2.315	2.260
S*(eV)*$^{-1}$	0.327	0.202	0.249	0.333	0.432	1.480
ω (eV)	4.085	2.869	4.183	3.523	2.901	4.323

be attributed to the electronic transition S_1 (first excited singlet state) → S_0 (ground singlet state) + $h\nu_{ph}$ (accompanied phonon energy) $S_1 \rightarrow S_0 + h\nu_{ph}$ (accompanied phonon energy). The other short-wavelength emission band detected at 591.5 nm can be assigned to the transition of S_2(the second excited singlet state)–S_0. The enhancement of the emission intensity may be attributed to the oscillator strength that is affected by the crystallinity and the mean particle size as described by Huang et al. [59].

3.6. The calculated and experimental electronic absorption spectra

The investigation of the electron transitions of PaOEP, TD-DFT calculations was achieved using polar and non-polar solvents of Q-and S-bands of the PaOEP structure. The absorption bands of PaOEP in all the desired solvents are shown in Fig. 9 and their assignments are recorded in Table 7. The calculated positions of the expected excitation, oscillator strength, and electron transition configurations are also listed in the table. The PaOEP spectra are strongly absorbed through the Soret region at around 3.58 V and the recorded Q-band at ~ 2.46 eV. The absorption band that corresponds to the maximum absorption of the PAOEP ring is red-shifted by 3–4 nm under the influence of solvent types. Table 7 lists the calculated excitation energies and the corresponding oscillator strengths of PaOEP in comparison with those published by a similar structure in the literature [60–64]. The obtained parameters of PAOEP agree with those obtained for comparable structures, which approves the precision of the achieved results.

The calculated Q bands of the absorption spectra of PaOEP in the gas phase were recorded at ~560 nm, whereas in benzene, hexane, and dichloromethane, acetone solvents are detected at 556, 557, 554, 553 nm, respectively. The Vis absorption bands can be assigned to the transition of n-π^*, π–π^*. The first state is localized in the Octaethyl porphyrin ring while the highest state is localized in the position of Pd^{+2}, Fig. 9. On this basis, the PaOEP is predictable to have high optoelectronic efficiency characteristics through photoinduced processes. The insertion of the Pd-metal atom and octaethyl moiety substitution further affect the absorption bands and useful for applications throughout the NIR -Vis range.

The experimental UV–visible absorption coefficient,α spectrum of highly conjugated PaOEP macrocycle thin films is shown in Fig. 10**(a)**. The figure shows that the structure displays a high intense peak centered at about 400 nm (i.e. Soret band), in agreement with those obtained theoretically by TD-DFT (extinction coefficient > 300.000 $mol^{-1}.cm^{-1}$. L). This band can be ascribed to the transition of the charge carrier from the ground level to Pt^{+2} -to-the state of the ligand (i.e., charge transfer singlet state [65–67]. Moreover, the minor peak at 555.2 nm and the shoulder centered at 518.4 nm (Q- bands) can be assigned to the transition from Pd^{+2} to the state of the ligand (i.e., charge-transfer spin-triplet state) [65–67]. The absorption spectrum investigation offers valuable supplementary evidence concerning the energy band and the optical transition type.

For obtaining useful information for the applicability of PaOEP for the application of optoelectronic devices, the evaluation of the energy bandgap and the predominant type of transitions should be considered. The analysis of α at the edge of absorption can be used for obtaining the energy bandgap, E_g with direct allowed transition as follows [68]:

$$(\alpha h\nu)^2 = A(h\nu - E_g) \quad (3)$$

where A is a constant. The plot of $(\alpha h\nu)^2$ vs. $h\nu$ is employed in Fig. 10**(b)** to confirm the type of transition and obtaining the energy gap of PaOEP films. This figure confirms that the predominant type of transition is the direct allowed with energy gaps of 2.23 eV for the onset energy gap (i.e. the minimum energy essential to pro-

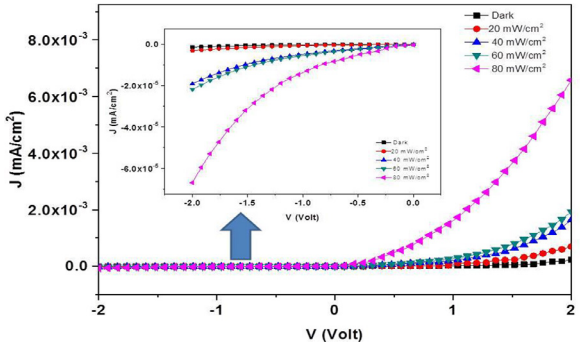

Fig. 12. Plot of J vs. V and the iset shows the reverse J-V characteristics of Au/ PaOEP /p-Si /In heterojunction.

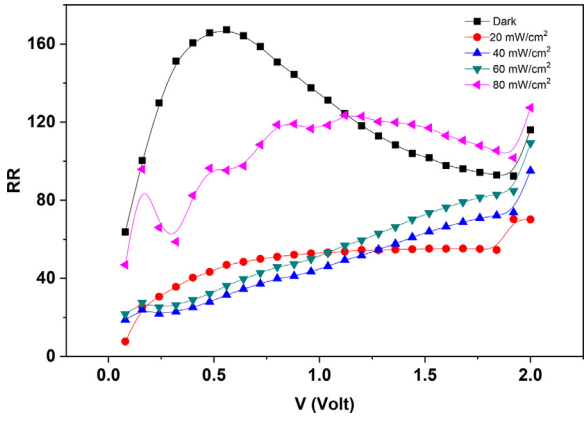

Fig. 13. Plot of RR vs. V characteristics of Au/ PaOEP /p-Si /In heterojunction.

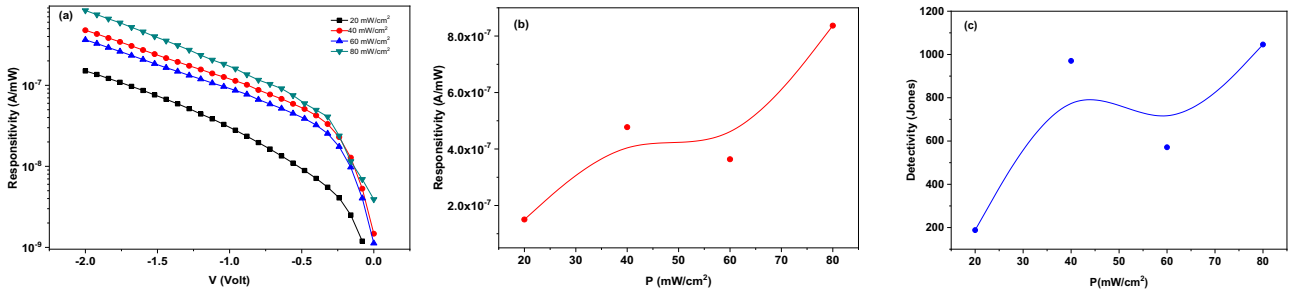

Fig. 14. Plots of (a) Responsitivity vs. V, (b) Responsitivity vs. P, and (c) Detectivity vs. P characteristics of Au/ PaOEP /p-Si /In heterojunction.

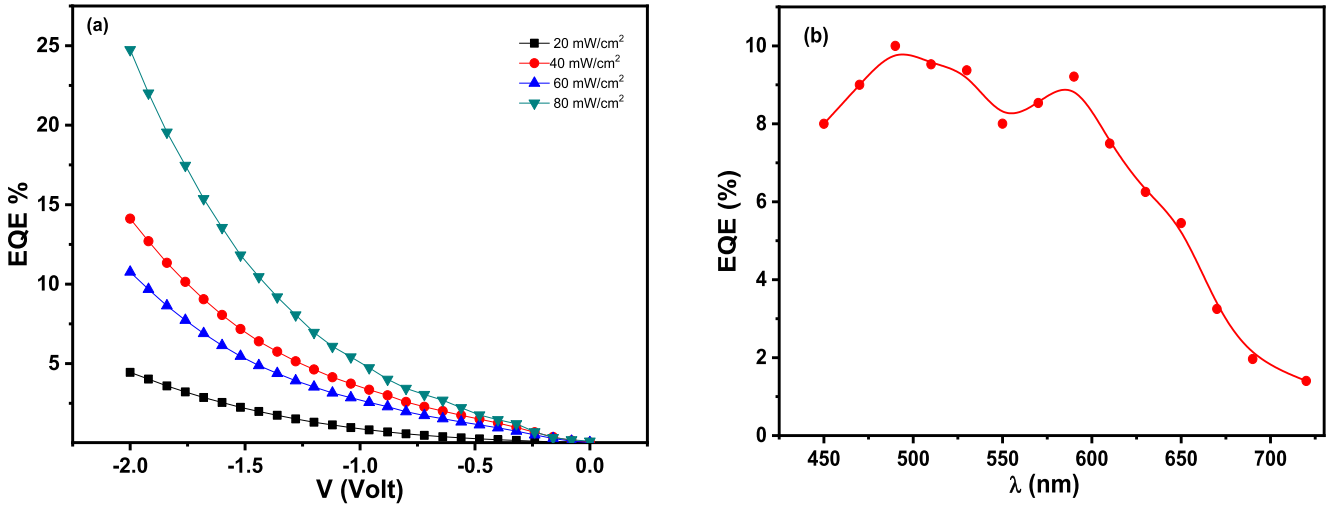

Fig. 15. (a) Plot of EQE vs. V, and (b) Plot of EQE vs. λ characteristics of Au/ PaOEP /p-Si /In heterojunction.

duce an electron-hole pair) [69] and 2.98 eV for the fundamental energy gap(i.e. HOMO-LUMO gap) [70]. The little disagreement between the experimental energy gap (2.98) and the theoretical energy gap (3.05) can be understood by ignoring the theoretical calculations for the molecular interactions by the neighbor molecules [71].

3.7. Dark and illuminated electrical properties

The schematic diagram of Au/ PaOEP /p-Si /In heterojunction structure is illustrated in Fig. 11. The electrical characteristics of Au/ PaOEP /p-Si/In heterojunction device are studied using the semi-logarithmic J-V curves is shown in Fig. 12. The measurements were considered in the dark and under illuminations in the range of 20–80 mW/cm^2. The heterojunction device displays remarkable rectification characteristics as shown from the comparison between the forward (Fig. 11) and reverse current (the inset of Fig. 12) under the same influence of bias. The potential dependence of the rectification ratio, RR is shown in Fig. 13. The figure shows an extraordinary RR in the dark condition and reaches its maximum value of 165 at 0.5 V. The increment in the reverse current under the influence of illumination is attributed to the production of excitons as a result of the absorption of light. The excitons are separated and swept away under the impact of built-in potential through the depletion region, creating the photocurrent [72,73].

To check the applicability of the PaOEP heterojunction device measure the sensitivity of the PaOEP heterojunction device, the main parameter should be studied are the responsivity, *R*, and the detectivity, *D*. The responsivity of the heterojunction device is related to the photocurrent density, J_{ph}, and the incident power of light, *P* using the following relation [74,75]:

$$R = \frac{J_{ph}}{P} \tag{4}$$

The reverse-biased dependency of the responsivity of the PaOEP heterojunction device under the illumination intensity range of 20–80 mW/cm^2, depicted in Fig. 14**(a)**, indicates an increase of R with increasing the applied reverse bias. Moreover, Fig. 13(b) confirms the high value of R as the intensity of illumination increases and consistent with the published results by Farag et al. [74] and El-Samahi et al. [71].

Besides, the detectivity of the heterojunction device, D is associated with the responsivity, R using the following formulation [74,75]:

$$D = \frac{R}{\sqrt{2qJ}} \tag{5}$$

The change of D of the heterojunction device based PaOEP diode with the variation in the illumination intensity is shown in Fig. 14**(c)**. This figure confirms the improvement of the detectivity by increasing the illumination intensity. The results obtained for the detctivity are consistent with those published by Farag et al. [73], Samahi et al. [74], and Abdel-Khalek [75]. The external quantum efficiency, EQE is an important measurement employed to detect the performance of the optoelectronic device in a wavelength range, λ and determined by the following [75]:

$$EQE = \frac{Rhc}{e\lambda} \tag{5a}$$

The variation of the EQE vs. the reverse bias of the PaOEP heterojunction device under various illuminations, Fig. 15**(a)**, designates a decreasing of EQE with increasing the applied bias and increases with increasing the illumination intensity inconsistent with

those reported by El-Samahi et al. [75]. Besides, the variation of EQE vs. wavelength, λ is shown in Fig. 15**(b)** to describe the heterojunction device's efficiency at each photon energy level. The figure shows that the PaOEP heterojunction device exhibits the highest EQE of 10% at λ of 500 nm. Furthermore, the EQE curve has a broad curve including a wide range of λ signifying that the PaOEP heterojunction device can be applicable for photosensitive device applications.

4. Conclusions

An evacuated thermally evaporating system was successfully employed to produce PaOEP thin films. The results of XRD and the Rietveld improvement data confirm that PaOEP has a nature of polycrystalline nature with a triclinic system and is supported by the results of SAED. The absorption spectrum of PaOEP thin films shows two characteristic bands called Soret and Q-bands. The spectrum analysis of absorption nearby the band edge of the films supports a direct allowed transition with energy gaps of 2.23 and 2.98 eV. The TD-DFT analysis for the absorption spectra in various polarity solvents spectra of the PaOEP shows specific Soret and visible transitions of 3.58 eV and 2.46 eV, respectively. The natural population analysis of the PaOEP structure showed a distribution of that 334 electrons. As a result, all coordination **Pd–N** bond occurring in the studied complex PaOEP in the ground state is characterized by the following conditions: $\nabla^2\rho(r) > 0$, and $h_e(r) < 0$ that determine an intermediate type of interaction in the framework of Bader's theory formalism. All the studied complexes are predicted to be very stable because of the high values of ion-to-ligand binding energies. The heterogeneous device based PaOEP thin films displays remarkable rectification properties. The heterojunction devices exhibit a broad curve the spectral dependence of and recorded the highest EQE of 10% at λ of 500 nm. The responsivity of the PaOEP heterojunction device and the results of EQE under influence of illumination candidates can be applicable for photosensitive device applications.

Declaration of Competing Interest

The authors declare that they have no known competing financial interests or personal relationships that could have appeared to influence the work reported in this paper.

CRediT authorship contribution statement

A.A.M. Farag: Conceptualization, Formal analysis, Investigation, Supervision, Writing - original draft. **N. Roushdy:** Data curation, Formal analysis, Methodology, Validation, Writing - review & editing. **Shimaa Abdel Halim:** Conceptualization, Formal analysis, Software, Visualization, Writing - review & editing.

Acknowledgments

The authors would like to thank the Physics and Chemistry Departments, Faculty of Education Ain Shams University, as well as Electronics Materials Dep. Advanced Technology& New Materials Research Inst., City of Scientific Research & Technological Applications (SRTA-City), New Borg El-Arab City, Alexandria, Egypt for supporting the scientific results.

References

[1] Hafiz Muhammad Asif, Arshad Iqbal, Yunshan Zhou, Lijuan Zhang, Ting Wang, Muhammad Inam Ullah Farooqi, Ran Sun, Preparation, characterization, and third-order optical nonlinearities of looped covalently bonded Anderson-type polyoxometalate-porphyrin hybrids, Dyes Pigments 184 (2021) 108758.
[2] C. Zhong, C. Duan, F. Huang, H. Wu, Y. Cao, Materials, and devices toward fully solution-processable organic light-emitting diodes, Chem. Mater. 23 (2010) 326–340.
[3] Francesca Bryden, Ross W. Boyle, Insights from Imaging in Bioinorganic Chemistry, Adv. Inorg. Chem. 68 (2016) 141–221.
[4] M.M. El-Nahass, H.S. Metwally, H.E.A. El-Sayed, A.M. Hassanien, Electrical and photovoltaic properties of FeTPPCl/p-Si heterojunction, Synth. Met. 161 (2011) 2253–2258.
[5] Y. Guo, E. Chen, E Yang, Q. Lin, Optical limiting properties of metalloporphyrin-based zirconium-polyphenolate frameworks, J. Solid State Chem. 285 (2020) 121224.
[6] X. Huang, F. Wei, F. Guo, Y. Zhu, Synthesis, crystal structure, and nonlinear optical properties of ferrocene-containing metalloporphyrins, Inorg. Chim. Acta 511 (2020) 119816.
[7] C. Sanchez, B. Julian, P. Belleville, M. Popall, Applications of hybrid organic-inorganic nanocomposites, J. Mater. Chem. 15 (2005) 3559–3592.
[8] Xi Chen, Yang Xu, Huanrong Li, Lanthanide organic/inorganic hybrid systems: efficient sensors for fluorescence detection, Dyes, and Pigments 178 (2020) 108386.
[9] M.M. El-Nahass, H.M. Zeyada, M.S. Aziz, M.M. Makhlouf, Current transport mechanisms and photovoltaic properties of tetraphenylporphyrin/n-type silicon heterojunction solar cell, Thin Solid Films 492 (2005) 290–297.
[10] M.M. El-Nahass, A.F. El-Deeb, H.S. Metwally, H.E.A. El-Sayed, A.M. Hassanien, Influence of X-ray irradiation on the optical properties of iron (III) chloride tetraphenylporphyrin thin films, Solid State Sci 12 (2010) 552–557.
[11] M.M. El-Nahass, H.S. Metwally, H.E.A. El-Sayed, A.M. Hassanien, Electrical and photovoltaic properties of FeTPPCl/p-Si heterojunction, Synth. Met. 161 (2011) 2253–2258.
[12] C. CastellarinCudia, P. Vilmercati, R. Larciprete, C. Cepek, G. Zampieri, L. Sangaletti, S. Pagliara, A. Verdini, A Cossaro, L. Floreano, A. Morgante, L. Petaccia, S. Lizzit, C. Battocchio, G. Polzonetti, A. Goldon, Electronic structure and molecular orientation of a Zn-tetra-phenyl porphyrin multilayer on Si(1 1 1), Surf. Sci. 600 (2006) 4013–4017.
[13] Xiao-Lei Zhang, Jian-Wei Jiang, Yi-Ting Liu, Shi-Tao Lou, Chun-Lei Gao, Qing-Yuan Jin, Identifying the Assembly Configuration and Fluorescence Spectra of Nanoscale Zinc-Tetraphenylporphyrin Aggregates with Scanning Tunneling Microscopy, Sci. Reports 6 (2016) 22756.
[14] Mannix P. Balanay, Dong Hee Kim, DFT/TD-DFT molecular design of porphyrin analogs for use in dye-sensitized solar cells, Phys. Chem. Chem. Phys. 17 (2013) 431–439.
[15] G.M. Youssef, M.M. El-Nahass, S.Y. El-Zaiat, M.A. Farag, Effect of porosity on the electrical and photoelectrical properties of textured n+ p silicon solar cells Mater, Sci. Semicond. Proc. 39 (2015) 457–466.
[16] (a) A.D. Becke, Density-functional thermochemistry, III: the role of exact exchange, J. Chem. Phys. 98 (1993) 5648–5652; (b) A.D. Becke, A new mixing of Hartree–Fock and local density-functional theories, J. Chem. Phys. 98 (1993) 1372–1377.
[17] S.H. Vosko, L. Wilk, M. Nusair, Can. Accurate spin-dependent electron liquid correlation energies for local spin density calculations: a critical analysis, J. Phys. 58 (1980) 1200–1211.
[18] (a) C. Lee, W. Yang, R.G. Parr, Development of the Colle-Salvetti correlation-energy formula into a functional of the electron density, Phys. Rev. B Condens. Matter 37 (1988) 785–789; (b) B. Miehlich, A. Savin, H. Stolt, H. Preuss, Chem. Phys. Lett. 157 (1989) 200–206.
[19] T. Schaefer, T. A.Wildman, S.R. Salman, The perpendicular conformation of 2-hydroxythiophenol. Intramolecular hydrogen bonding to a specific lone pair, J. Am. Chem. Soc. 102 (1980) 107–110.
[20] T. Schaefer, S.R. Salman, T.A. Wildman, P.D. Clark, Conformational consequences of intramolecular hydrogen bonding by OH to the directional lone–pair of sulfur in derivatives of methyl phenyl sulfide, diphenyl sulfide, and diphenyl disulfide, Can. J. Chem. 60 (1982) 342–352.
[21] A.D. Becke, Density-functional thermochemistry. III. The role of exact exchange, J. Chem. Phys. 98 (1993) 5648–5652.
[22] P.J. Hay, W.R. Wadt, Ab initio effective core potentials for molecular calculations. Potentials for main group elements Na to Bi, J. Chem. Phys. 82 (1985) 270–280.
[23] R.A. Gaussian, M.J. Frisch, G.W. Trucks, H.B. Schlegel, G.E. Scuseria, M.A. Robb, J.R. Cheeseman, G. Scalmani, V. Barone, B. Mennucci, G.A. Petersson, et al., Gaussian, Inc., Wallingford CT, 2009.
[24] R. Dennington, T. Keith, J. Millam, Gauss View, Version 5 Semichem Inc., Shawnee Mission, KS, 2009.
[25] G.A. Zhurko, D.A. Zhurko, Chemcraft (2005) http://www.chemcraftprog.com.
[26] T. Yanai, D. Tew, N. Handy, A new hybrid exchange-correlation functional use the Coulomb-attenuating method (CAM-B3LYP), Chem. Phys. Lett. 393 (2004) 51–57.
[27] C.L. Firme, O.A.C. Antunes, P.M. Esteves, Relation between bond order and delocalization index of QTAIM, Chem. Phys. Lett. 468 (2009) 129.
[28] F. Shahangi, A.N. Chermahini, H. Farrokhpoura, A. Teimouri, Selective complexation of alkaline earth metal ions with nanotublar cyclopeptides:DRT theoretical study, RSC Adv 5 (2015) 2305–2317.
[29] D. Cremer, E. Kraka, A Description of the Chemical Bond in Terms of Local Properties of Electron Density and Energy, Croat. Chem. Acta 57 (1984) 1259–1281.
[30] S.F. Boys, F. Bernardi, The calculation of small molecular interactions by the differences of separate total energies. Some procedures with reduced errors, Mol. Phys. 19 (1970) 553–566.

[31] T.A. Keith, www.aim.tkgristmill.com, (2010).
[32] H. Mizuseki, K. Niimura, C. Majumder, R.V. Belosludov, A.A. Farajian, Y. Kawazoe, Electronic properties of magnetically doped nanotubes, Mol. Cryst. Liq. Cryst. 406 (2003) 195–204.
[33] R. Neil, Angew Synthetic multivalent ligands as probes of signal transduction, Chem. Int. Ed. 45 (2006) 2338–2345.
[34] L. Armelao, S. Quici, F. Brigelletti, G. Accorsi, G. Bottaroi, M. Cavazzini, E. Tendello, Synthesis, and spectroscopic characterization of new tetradentate Sciff base and its coordination compounds of non-doner atoms and their antibacterial and antifungal activity, Arab. J. Chem. 3 (2010) 103–113.
[35] A.I. Boldyrev, V.V. Zhdankin, J. Simons, P.J. Stang, Intramolecular energy flow and bond dissociation in iodoacetylene and iododiacetylene, J. Chem. Phys. 101 (1994) 4668.
[36] J.S. Murray, K. Sen, Electronic Molecular Structure, Reactivity, and Intermolecular Forces: an Euristic Interpretation utilizing Electrostatic Molecular Potentials, Adv. Quant. Chem. 11 (1996) 115–193.
[37] F.J. Luque, J.M. López, M. Orozco, Perspective on Electrostatic interactions of a solute with a continuum. Direct utilization of ab initio molecular potentials for the prevision of solvent effects, Theoret. Chem. Accounts. 103 (2000) 343–345.
[38] N. Okulik, A.H. Jubert, Theoretical Analysis of the Reactive Sites of Non–steroidal Anti-inflammatory Drugs, Internet Electron. J. Mol. Des. 4 (2005) 17–30.
[39] P. Politzer, J.S. Murray, The fundamental nature and role of the electrostatic potential in atoms and molecules, Theor. Chem. Acc. 108 (2002) 134–142.
[40] D.L. Wang, H.T. Shen, H.M. Gu, Y.C. Zhai, Molecular Electrostatic Potential as a Tool for Evaluating the Etherification Rate Constant, J. Mol. Struct. 776 (2006) 47–51.
[41] G. Naray-Szabo, G.G. Ferenczy, Molecular Electrostatics, Chem. Rev. 95 (1995) 829–847.
[42] N.N. Karaush, G.V. Baryshnikov, B.F. Minaev, RSC Adv., 5 (2015) 24299.
[43] J. Heo, Theoretical Studies on Selectivity of Dibenzo-18-Crown-6-Ether for Alkaline Earth Divalent Cations, Bull. Korean Chem. Soc. 33 (2012) 2669–2674.
[44] T.Y. Cho, C.W. Han, Y. Jun, S.G. Yoon, Formationofartificialporesinnano-TiO_2 photo-electrode films using acetylene black for high-efficiency, dye-sensitized solar cells, Sci. Rep. 3 (2013) 1496–1511.
[45] A.A.M. Farag, Shimaa Abdel Halim, N. Roushdy, Al-Shimaa Badran, Magdy A Ibrahim, Facile synthesis and photodetection characteristics of novel nanostructured triazinyliminomethylpyrano [3,2-c]quinoline-based hybrid heterojunction, J.Mol. Struct. 1221 (2020) 128868.
[46] A. Belfedal, D. Benlakehal, Y. Bouizem, R. Baghdad, M. Clin, A. Zeinert, O. Durand, Drouhin, J.D. Sib, L. Chahed, K. Zellama, Surface roughness and optoelectronic properties of intrinsic and doped nc-Si: h prepared by Rf-magnetron sputtering at low temperature, Mater. Sci. Semicond. Proc. 26 (2014) 231–237.
[47] T.Y. Cho, C.W. Han, Y. Jun, S.G. Yoon, Formationofartificialporesinnano-TiO_2 photo-electrode films using acetylene black for high-efficiency, dye-sensitized solar cells, Sci. Rep. 3 (2013) 1496–1511.
[48] A.A.M. Farag, Shimaa Abdel Halim, N. Al-Shimaa Badran, Magdy A. Ibrahim, Facile synthesis and photodetection characteristics of novel nanostructured triazinyliminomethylpyrano [3,2-c]quinoline-based hybrid heterojunction, Journal of Mol. Struct. 1221 (2020) 128868.
[49] A. Belfedal, D. Benlakehal, Y. Bouizem, R. Baghdad, M. Clin, A. Zeinert, O. Durand, Drouhin, J.D. Sib, L. Chahed, K. Zellama, Surface roughness and optoelectronic properties of intrinsic and doped nc-Si: h prepared by Rf-magnetron sputtering at low temperature, Mater. Sci. Semicond. Proc. 26 (2014) 231–237.
[50] R.A. Young, D.B. Wiles, Rietveld refinement of Debye-Scherrer synchrotron X-ray data from Al_2O_3, J. Appl. Cryst. 15 (1982) 430–438.
[51] V.D. Mote, Y. Purushotham, B.N. Dole, Williamson-Hall analysis in estimation of lattice strain in nanometer-sized ZnO particle, J. Theo. Appl. Phys. 6 (2012) 8-1.
[52] K. Mandal, T. Kar, P.K. Nandi, S.P. Bhattacharyya, Ab initio SCRF study of solvent effect on the nonlinear polarizabilities of different intramolecular charge–transfer molecules, Chem. Physics Lett. 376 (2003) 116–124.
[53] P.N. Prasad, D.J. Williams, Introduction to Nonlinear Optical Effects in Molecules and Polymers, John Wiley & Sons, New York, NY, USA, 1991.
[54] C.R. Zhang, H.S. Chen, G.H. Wang, DFT studies on the electronic structures of 4-methoxybenzonitrile dye for Dye-Sensitized Solar, Cell Chem. Res. Chin. U. 20 (2004) 640–646.
[55] Y.Y. Lin, N.P. Rajesh, P.S. Raghavana, P. Ramasamy, Y.C. Huang, Crystal growth of two-component new novel organic NLO crystals, Mater. Lett. 56 (2002) 1074.
[56] Mi-J. Lee, M.P. Balanay, D.H. Kim, Theor. Chem. Acc. 131 (2012) 1269–1278.
[57] M.A. Elistratova, I.B. Zakharova, N.M. Romanov, V. Yu. Panevin, O.E. Kvyatkovskii, Photoluminescence Spectra of Thin Films of ZnTPP–C60 and CuTP-P–C60 Molecular Complexes, Semicond. 50 (2016) 1191–1197.
[58] Gaobin Zhang, Qiyu Chena, Yuyang Zhang, Lin Kong, Xutang Tao, Hongbo Lu, Yupeng Tian, Jiaxiang Yang, Inorg. Chem. Commun. 46 (2014) 85–88.
[59] Y. Tachibana, S.A. Haque, I.P. Mercer, J.R. Durrant, D.R. Klug, Electron Injection and Recombination in Dye-Sensitized Nanocrystalline Titanium Dioxide Films: A Comparison of Ruthenium Bipyridyl and Porphyrin Sensitizer Dyes, J. Phys. Chem. B 104 (2000) 1198–1205.
[60] M.H. Huang, Y. Wu, H. Feick, N. Tran, E. Weber, P. Yang, Catalytic growth of zinc oxide nanowires by vapor transport, Adv. Mater. 13 (2001) 113–116.
[61] A.M. El Mahdy, Shimaa Abdel Halim, H.O. Taha, DFT and TD-DFT calculations of metallotetraphenylporphyrin and metallotetraphenylporphyrin fullerene complexes as potential dye sensitizers for solar cells, J. Mol. Struct. 1160 (2018) 415–427.
[62] J.M. Juma, S.A.H. Vuai, N.Surendra Babu, TD-DFT Investigations on Optoelectronic Properties of Fluorescein Day Derivatives in Dye-Sensitized Solar Cells (DSSCs), Hindawi, Inter. J. Photoenergy (2019) 1–8 2019.
[63] M. Ghosh, Shivraj, B. Siddlingeshwar, A. Thomas, S. Sinha, Non-Radiative Transitions in Metal-Free Octaethylporphyrin and 2-Nitrofluorene Donor-Acceptor System, ChemRxiv 4 (2018) 1–11.
[64] Xiao-Feng Wang, Osamu Kitao, Natural Chlorophyll-Related Porphyrins and Chlorins for Dye-Sensitized Solar Cells, Molecules 17 (2012) 4484–4497.
[65] Qian Liu, Penghui Ren, Xiaofei Wang, Yuanzuo Li, Yanhui Yang, Experimental and Theoretical Investigations of the Photoelectrical Properties of Tetrabromophenol Blue- and Bromoxylenol Blue-Based Solar Cells, Hindawi, J. Nanomater. (2018) 1–13 2018.
[66] Dolphin, The Porphyrins, I–VII, Academic Press, New York, 1978.
[67] A.A. Abuelwafa, A. El-Denglawy, M. Dongol, M.M. El-Nahass, T. Soga, Structural and optical properties of nanocrystalline platinum octaethylporphyrin (PtOEP) thin films, J. Alloys Compd. 655 (2016) 415–422.
[68] A.K. Bansal, W. Holzer, A. Penzkofer, T. Tsuboi, Absorption and emission spectroscopic characterization of platinum-octaethyl-porphyrin (PtOEP), Chem. Phys. 330 (2006) 118–129.
[69] M. Özçeşmeci, İ. Özçeşmecia, İ. Sorar, E. Hamuryudan, Thin films of fluorinated groups substituted metallophthalocyanines as an optical material, Inorg. Chem. Commun. 86 (2017) 209–212.
[70] E.V. Tsiper, Z.G. Soos, W. Gao, A. Kahn, Electronic polarization at surfaces and thin films of organic molecular crystals: PTCDA, Chem. Phys. Lett. 360 (2002) 47–52.
[71] U. Zhokhavets, R. Goldhahn, G. Gobsch, W. Schliefke, Dielectric function, and one-dimensional description of the absorption of poly(3-octylthiophene), Synth. Met. 138 (2003) 491–495.
[72] Y. Saeed, K. Zhao, N. Singh, R. Li, J.E. Anthony, A. Amassian, U. Scwingenschlgl, Influence of substitution on the optical properties of functionalized pentacene monomers and crystals: experiment and theory, Chem. Phys. Lett. 585 (2013) 95–100.
[73] A.A.M. Farag, Shimaa Abdel Halim, N. Roushdy, Al-Shimaa Badran, Magdy A. Ibrahim, Facile synthesis and photodetection characteristics of novel nanostructured triazinyliminomethylpyrano [3,2-c]quinoline-based hybrid heterojunction, J. Mol. Struct. 1221 (2020) 128868.
[74] M.I. El-Samahi, H. Abdel-Khalek, Mohamed Abd-El Salam, Ahmed M El-Mahalawy, Fabrication and performance evaluation of ultraviolet photodetector based on organic /inorganic heterojunction, Curr. Appl. Phys. 18 (2018) 1496–1506.
[75] H. Abdel-Khalek, E. Shalaan, M. Abd-El Salam, A.M. El-Mahalawy, Effect of illumination intensity on the characteristics of $Cu(acac)_2$/n-Si photodiode, Synth. Met. 245 (2018) 223–236.